Preprint of: Szmytkowski J., Galagan Y., Głowienka D., Exploring the interfacial effects at the ETL/perovskite boundary in the semitransparent perovskite solar cells, SOLAR ENERGY, Vol. 266 (2023), 112176, DOI: 10.1016/j.solener.2023.112176

Exploring the interfacial effects at the ETL/perovskite boundary in the semitransparent perovskite solar cells

Jędrzej Szmytkowski[a,], Yulia Galagan[b], Damian Glowienka[a]

[a] *Faculty of Applied Physics and Mathematics, Gdańsk University of Technology, Narutowicza 11/12, 80-233 Gdańsk, Poland*
[b] *TNO, 5656 AE Eindhoven, Netherlands*

Abstract

The recent focus has been made on the perovskite solar cells (PSCs) with an inverted configuration, where substantial improvements have been already achieved. However, the *p*–*i*–*n* structure needs a buffer layer for most of the configurations to modify the work–function of a deposited electrode. Additionally and very importantly, such a layer can also serve as a protective film that improves a stability of solar cells. Here, we study the semitransparent inverted PSCs, which have been prepared with the SnO_2 buffer layer deposited by a spin–coating method. The main goal was to understand the dominant loss mechanisms in the operation of PSCs. Four photovoltaic parameters (an open–circuit voltage, a short–circuit current, a fill factor and a power conversion efficiency) were measured for a wide range of the light intensity. Their analysis allowed us to identify the transportation and recombination effects using an electrical modeling based on the drift–diffusion model. In addition, it has been concluded that the solution processed PCBM layer might not fully cover the perovskite film. As a consequence, the band–bending effect can occur at the PCBM/perovskite interface, where PCBM plays a role of the Electron Transpot Layer (ETL). Therefore, we theoretically investigated the influence of this interface phenomenon on four photovoltaic parameters and the ideality factor simulated as a function of the ETL interface defect density. The increasing

Email addresses: jedszmyt@pg.edu.pl (Jędrzej Szmytkowski), damian.glowienka@pg.edu.pl (Damian Glowienka)

of the ideality factor to a high value (above 4) observed for the band–bending level around 300 eV indicates inhomogeneity of the interface. The results of this study should help to better understand the dominant electrical losses in the semitransparent inverted PSCs with a buffer layer which should further help to improve the performance of such devices.

Keywords: Photovoltaics, Renewable Energy, Perovskite Solar Cells, Energy Efficiency, Buffer Layer

1. Introduction

World energy consumption still increases and it leads to the development of different types of energy sources. Photovoltaics seems to be a very promising form of a renewable energy. Still, solar cells based on crystalline silicon (c–Si) or amorphous silicon (a–Si) are very popular for the conversion of a sunlight into electricity [1]. However, other semiconductors such as gallium arsenide (GaAs) [2] or cadmium telluride (CdTe) [3] can be also used to produce efficient photovoltaic devices. The other effective compound is $CuIn_xGa_{1-x}Se_2$ (CIGS) [4], where cadmium sulfide (CdS) often plays a role of the buffer layer [5, 6].

Although photovoltaic panels based on these materials are already used in a daily life, there is a need to find more efficient or cheaper compounds to fabricate solar cells. The class of high absorbing semiconductors Cu_2XSnS_4 (X = Fe, Co, Ni, Cu, Zn, Mn) seems to become an alternative to the CIGS system [7, 8, 9, 10]. In addition, researchers try to find optical transparent materials to use them in semitransparent solar cells. Good candidates are Sb_2S_3 and Sb_2Se_3 characterized by a wide band gap [11, 12]. In recent decades, photovoltaic devices with organic materials (like donor–acceptor structures [13] and hybrid dye–sensitized solar cells [14]) have attracted a lot of attention. The reason is a low manufacturing cost and possibility to obtain flexible solar cells.

The other type of promising photovoltaic devices are perovskite solar cells (PSCs). Here, we can distinguish hybrid organic–inorganic PSCs [15, 16, 17]. They are recently getting attention due to the outstanding increase in power

conversion efficiency (PCE), which is already reaching over 20% [18]. It is believed that lead halide PSCs will deliver a very low cost of solar energy (< 32 \$ per MWh) [19]. In addition, efficient semitransparent PSCs have been fabricated using hybrid organic–inorganic perovskites [20, 21, 22], which increases their attractiveness. However, we also observe intensive studies of all–inorganic PSCs [23, 24, 25, 26, 27].

At the beginning of the PSCs development, the *n–i–p* (regular planar) stack has been more often used due to achieving higher efficiencies [28]. Here, n is the n–type semiconductor and represents an Electron Transport Layer (ETL), i denotes an undoped intrinsic semiconductor which is a perovskite absorber layer, and p represents the p–type semiconductor called a Hole Transport Layer (HTL). However, further studies have indicated problems with PSCs with a regular layout mostly due to the transport layers which are sensitive to a moisture [29] and thermal stresses [30]. Therefore, the recent focus has been made on the *p–i–n* (inverted planar) stack to see if there are new possibilities for improving the PSC's efficiency and stability [31].

One of the very important aspects of an inverted stack is the need for a buffer layer to improve the contact with the metal collecting electrode depending on its work–function. The most preferred used buffer material is organic bathocuproine (BCP) [28, 32]. However, there are also attempts to apply a very thin layer of LiF [33, 34], polyethylenimine (PEIE) [35] or tris(8–hydroxyquinolinato)aluminum (Alq_3) [36]. The usage of these compounds has its own advantages and, in general, increases the efficiency of PSCs. However, it does not improve a stability of the solar cells against the oxygen and the moisture from an environment [37]. Thus, one of the solutions on that is to apply a dense buffer layer that would protect the absorber material.

Theoretically, there should be no interaction between the buffer and the absorber layers due to the ETL sandwiched in between. Therefore, one can believe that a role of the buffer layer can be only limited to the work–function modification and stability improvement. However, a solution process is still the most frequently used technique for making ETL and it might not be able to fully

cover a perovskite layer. This seems to be extremely important if considering a manufacturing process, where a large area perovskite film has to be covered with the ETL [40]. Especially, since the morphology of a perovskite layer might depend on the used solvents [41] or a perovskite composition [42]. Therefore, there is a need to recognize all effects which can occur at the ETL/perovskite interface in the presence of a buffer layer.

Here, we investigate the influence of the buffer layer created from the solution processed SnO_2 nanoparticles. The PSCs have been prepared in the semitransparent p–i–n stack with glass/ITO/PTAA/perovskite/PCBM/SnO_2/ITO configuration. Here, ITO is the tin–doped indium oxide, PTAA denotes poly(triaryl amine), whereas PCBM represents [6,6]–phenyl–C_{61}–butyric acid methyl ester. Our studies are supported by experimental and theoretical investigations. Therefore, PSCs are measured under different light intensities with the current–voltage (J–V) characterization to examine the dominant effects using the drift–diffusion numerical model [43]. Also, the device's bifaciality due to the usage of two ITO electrodes allowed us to measure samples illuminated from both sides. Meaning, more physical effects can be considered in the model, thereby making the simulations much more accurate. We should mention that, as to our knowledge, the interfacial processes occuring at the ETL/perovskite boundary have not been widely investigated for the semitransparent PSCs with a buffer layer. In addition, the influence of the interface band–bending effect, which might appear at this boundary, has not been deeply analyzed in such a structure.

2. Materials and methods

2.1. Device fabrication

In order to prepare a precursor for the perovskite $Cs_{0.15}FA_{0.85}Pb(I_{0.98}Br_{0.02})_3$ solutions, the following chemicals have been used: lead iodide (PbI_2, 99.99%, TCI), formamidinium iodide (FAI, GreatCell Solar), caesium iodide (CsI, 99.999%, Alfa Aesar), caesium bromide (CsBr, 99.999%, Alfa Aesar), dimethylformamide (DMF) solvent (99.8%, Sigma–Aldrich) and 1–methyl–2–pyrrolidinone (NMP)

solvent (99.5%, ACROS Organics). We did not purify these commercial compounds. The amounts: 1.4M PbI_2, 1.19M FAI, 0.126M CsI and 0.084M CsBr have been applied to produce the precursor. The prepared compositions have been dissolved in a solvent mixture (DMF:NMP, 9:1 volume ratio). Later, the solutions were stirred overnight at room temperature.

The substrates for solar cells made from the patterned glass/ITO were ultrasonically cleaned and, additionally, UV–ozone treated for 30 min. The N_2–filled glove–box (with the oxygen and the moisture levels at about 1 ppm) has been used to fabricate PSCs. The HTL layer was created by a spin–coating method using 4 mg mL^{-1} of PTAA (Solaris M) solution dissolved in toluene (at 5000 revolutions per minutes (RPM) for 35 s and with an acceleration equal to 5000 RPM s^{-1}). Next, the samples were annealed for 10 min at a temperature of 100°C. Further, the gas quenching method [45] has been applied for a dynamical spin–coating of the precursor solution (150 µL). To obtain the desired thickness of a perovskite material, a two–step program was used: firstly, 2000 RPM rotational speed for 10 s with an acceleration 200 RPM s^{-1}, and secondly, 5000 RPM for 30 s with 2000 RPM s^{-1}. After 15 s of this spin–coating process, a gun with nitrogen (at 6 bars pressure) located at 10 cm vertical distance from the substrate has been used for quenching of the perovskite layer for 15 s. Immediately after the quenching, the samples were annealed at 100°C for 10 min on the hot–plate. The solution for ETL (20 mg mL^{-1}) has been created with PCBM (99%, Solenne) dissolved in a chlorobenzene solvent. This solution was stirred overnight at 60°C. Subsequently, it was spin–coated on the samples with a speed 1500 RPM for 50 s and 3000 RPM s^{-1} acceleration. Later, the solution made from SnO_2 nanoparticles (Avantama N–31) 2.5 wt% in a mixture with a butanol filtered with 0.2 µm polypropylene filter has been prepared. It was used to create the next layer by a spin–coating process (3000 RPM speed for 50 s and 3000 RPM s^{-1} acceleration). Further, the samples were annealed on the hot–plate (at 80°C for 5 min).

Afterward, ITO prepared for the second electrode was cleaned in the air with DMF:chlorobenzene solution (1:6 volume ratio). The ITO material, character-

ized with a sheet resistance equal to 22±2 Ω/□, has been deposited at room temperature with the radio frequency (RF) magnetron sputtering [46] (AJA Sputtering System) to create a 180 nm layer. At last, metal electrical contacts with a thickness of 100 nm have been prepared by the thermal deposition technique under the pressure of 10^{-6} mbar.

2.2. Experimental and theoretical methods

The crystal structure of perovskite films was characterized with a Bragg–Brentano geometry X–ray diffractometer (XRD) from PanAlytical Empyrean, whereas the atomic force microscope (AFM) with the Park NX–10 tool was used to study the morphology of the perovskite material. The Bruker XT Dektak profilometer has been applied to measure thicknesses of all layers.

The J–V characteristics of PSCs have been recorded using Keithley 2400. These measurements were conducted in N_2 environment under a white light halogen lamp simulating the standard Air Mass 1.5 (AM1.5) spectrum with a light intensity calibrated to 1 sun (100 mW cm^{-2}) using a silicon reference cell. The illuminated cells had active areas equal to 0.09 cm^2. For the light intensity studies, the neutral filters have been used to achieve 0.001, 0.01, 0.1, 0.33, 0.53, 0.83 and 1 sun. All the J–V characteristics were recorded with a scanning rate of 0.165 V s^{-1} with 20 mV step and with 2 minutes of light soaking preconditioning. In order to analyze the hysteresis effect, the scanning direction has been performed firstly in the reverse (from 1.2 V to -0.2 V) and then in the forward (from -0.2 V to 1.2 V) applied voltage directions. The measurement setup combined with two different holders for the front and the rear side of illumination has been used to measure the external quantum efficiency (EQE). To find the maximum power point tracking (MPPT), the representative solar cell was continuously illuminated for about 2 minutes with the control of voltage and current.

To simulate the PSCs, we have decided to apply the drift–diffusion model which was explained in details in our previous studies [43]. With the use of continuity equations for electrons and holes, it quantitatively describes the mecha-

nisms of the generation, the transport and the recombination of charge carriers. The Shockley–Read–Hall, the modified Langevin and the Auger effects are the dominant recombination processes in the considered system. Here, we have not taken into account the migration of ions. The reason is that an influence of ions on the operation of PSCs is negligible for steady–state conditions [44]. The Scharfetter–Gummel method with the Chebyshev polynomials has been used for the discretization of the applied model [43]. To not neglect energy differences, which might occur between layers in a solar cell, the full PSC stack has been studied with the method of generalized potentials [47, 48, 49]. A fitting procedure has been done with the differential evolution algorithm [38, 50] to find a global minimum, and also with the Nelder–Mead model [51, 52] for further optimization. For both algorithms, the Chi–Square test was used to define the goodness of fit. All simulations were performed using our own numerical code written in C++.

3. Results and discussion

3.1. Characterization of the semitransparent PSCs

The sandwich structure of investigated solar cells is presented in Fig. 1a. The PSCs have been prepared with the front (ITO on glass) and the rear (ITO) collecting electrodes in the *p–i–n* configuration. The PTAA serves as the HTL, whereas PCBM as the ETL. The thicknesses of HTL and ETL are equal to 14.01±2.00 nm and 40.95±1.83 nm, respectively. The double–cation (2C) perovskite $Cs_{0.15}FA_{0.85}Pb(I_{0.98}Br_{0.02})_3$ plays a role of the absorber with a thickness equal to 536.48±4.84 nm. The SnO_2 buffer layer (around 45 nm) is located between PCBM and the rear ITO electrode.

Fig. 1b shows the J–V characteristics of a representative solar cell. The photovoltaic parameters presented in Table 1 are calculated for the same PSC. It can be seen that the PCE reverse scan gives higher results by about 2% if compared to the forward scan. This is mostly due to the Fill Factor (FF) which has a value higher by approximately 4% for the reverse direction of the

measurements. It leads to a hysteresis effect which is often observed in PSCs [53]. The observed hysteresis has also slightly influenced an open–circuit voltage (V_{oc}) and a short–circuit current (J_{sc}), see Table 1. The Hysteresis Index (HI) [54] is different for samples measured from the front and the rear sides. HI has been calculated for 12 devices for each variation. It is equal to 0.083±0.015 and 0.075±0.014 for the front and the rear side, respectively. Thus, we observe a higher hysteresis for the front side of PSCs. The dissimilarity of HI from the front to the rear side could be related to the asymmetrical charge carriers distributions. The recent findings show that the hysteresis effect is most likely accounted for both, the transport of ionic charge carriers and the trap–assisted recombination [55].

The samples have been also measured with the EQE technique from both sides, see the results for the representative sample presented in Fig. 1c. The small differences are found to be batch–to–batch related probably due to a film thickness variation. Most of the optical losses for the front side at short wavelengths can be associated with the parasitic absorption of the ITO substrate [56]. However, the optical losses from the rear side at the same range of wavelengths are coming from PCBM and SnO_2 layers which highly absorb in the range from 300 nm to 500 nm [56, 57, 58]. The calculated J_{sc} from the integration of EQE is equal to 19.54 mA cm^{-2} for the front side of the sample. It shows the same trend observed in J–V measurements, thus qualifying our measurements.

Figs. 1d–g illustrate four photovoltaic parameters (PCE, J_{sc}, FF and V_{oc}) measured with illumination from the front and the rear sides. The bifacial factor is approximately equal to 88% for PSCs by statistical meaning. Interestingly, the differences from both side measurements are negligible. It could be also mentioned that FF has always a higher value for the front side if compared to the rear one, see Fig. 1f. It exhibits approximately 8% higher FF for samples.

To better understand the dominant mechanisms of operation, we have measured the representative PSC under different light illuminations in the range from 0.0001 suns to 1 sun. The obtained experimental results have been simulated using the drift–diffusion model under steady–state conditions. Table 2 in-

cludes all the simulation parameters used in the modeling. The values of quantities for the HTL (PTAA [59, 60, 61]) and for the ETL (PCBM [62, 63, 64, 65, 66]) have been taken from the literature. The electrical properties of the perovskite material were described in the reference [67] or were found from fitting to the experimental data [68, 69]. The very low charge carrier mobility equal to 0.003 $cm^2\ V^{-1}\ s^{-1}$ was obtained for SnO_2 material [70, 71]. However, its high intrinsic donor doping [72] equal to $10^{22}\ m^{-3}$ allows for negligible losses in the operation of PSCs. Also, the energetical levels are assumed to create a junction based on the Fermi levels of an intrinsic PCBM and a donor doped SnO_2. This shifts the conduction band of SnO_2 [73] from -4.5 eV by around 0.6 eV. Additionally, to calculate the generation profile, the optical transfer–matrix model has been applied [74, 75]. The optical real and imaginary refractive indices for PTAA, perovskite and PCBM were provided from our previous work [43], whereas these quantities for SnO_2 were adopted from the literature [76].

Fig. 2 shows the experimental and simulation results for the front and rear sides of the representative sample. The theoretical results match very well (R^2 coefficient of determination is equal to 93.3%) to the experiment in the short–circuit (SC) to the open–circuit (OC) range, and also above OC. This range of applied voltage is mostly related to diffusion currents which depend on the transport properties of the device. Therefore, a very good correlation has been possible to acquire only if using well–matching electrical parameters of all the layers. The same good correlation is observed for the front (Fig. 2a) and the rear (Fig. 2b) sides of measurements. The only discrepancy has been found for V_{oc} under different light illumination from the rear side which affects the precision of a fitting procedure. This might be explained by the ion migration effects [77] or multiple trap defects distributed at different energy levels [78, 79].

Fig. 3 illustrates the photovoltaic parameters for the same representative sample, where the correlation between the experiment and the simulations is presented for both illuminated sides. Fig. 3a shows the dependence of PCE on light intensity. We should notice that the bifacial factor changes for different intensities. It is equal to 90% for 1 sun and increases to 100% at 0.0001 suns.

The efficiency has always a higher value for the front side if compared to the rear side mostly in the FF and PCE values. This has been already observed in PSCs [80]. The experimental trend is again very well reproduced by the simulation results.

Fig. 3b shows the J_{sc} behavior as a function of the light intensity. It is observed that the photocurrent indicates a linear relationship in the log–log plot. This tendency has been already associated with monomolecular recombination as a dominant process that is here related to the trap–assisted recombination [81]. In the simulations, we apply the generation profile that is calculated separately for the front and the rear sides using the aforementioned transfer–matrix model. The stack in the optical model has been used exactly the same as in the experiment to get the model as close as possible to the experimental data. As it is visible, the photocurrent in light intensity results well matches the experimental values.

Fig. 3c shows the FF measured and simulated for different light intensities. This parameter is the most sensitive for simulations and only one possible set of parameters can cover such a wide range of light illumination for both measuring sides. Here, the simulations show a very good fit for the front and the rear sides. Thus, it gives a set of values that leads to a very precise fitting. As it has been already observed, FF is higher if measuring from the front to the rear side of the PSC. The same tendency can be seen for the light illumination studies, where FF differs from the front to the rear side by approximately 6% at 1 sun and reduces to zero for the lowest measured light intensities. This effect has been possible to reproduce with simulations only by adding a donor doping in the bulk of a perovskite layer. The self–doping affects the type of electronic conductivity making a perovskite of the n–type [82]. This intrinsic property of the perovskite material might be of high importance to fabricating tandem PSCs, where the light could illuminate the rear side [83].

Further, by analyzing the FF parameter in the function of light intensity, we can learn more about the impact of the trap–assisted recombination and also about the transport properties. A solar cell without any recombination or

transport losses would be characterized by a flat curve with a value equal to approximately 90% for all light intensities [84]. However, a real solar cell always possesses some losses caused by defects or low transport properties. Therefore, FF at around 85% at its peak value can be considered as a representation of a very good solar cell. Here, we observe a low value of FF around 70% at a high light intensity regime for the front side measurements. It is found that this is only present in the semitransparent PSCs which have a higher series resistance of the top electrode, see Table 2. However, the peak value of FF reaches approximately 75% at 0.01 suns for both sides of illumination. This loss is assigned to defect states in the bulk of the absorber layer which leads to the trap–assisted recombination. We have found the trap defect density equal to $(7.23\pm0.09)\times10^{21}$ m^{-3}, see Table 2. In general, values below 10^{22} m^{-3} are considered for a high quality perovskite film [85]. However, it should be also understood that this value shows an average representation of the trap distribution in the bulk. It has been already demonstrated by Ni et al. [86] that the distribution is non–linear with the highest trap densities at the interfaces. Thus, we separate both of the interfaces by giving two values of defect densities that resemble the non–linear defect distributions. For the sample, we have found almost symmetric defect densities equal to $(1.09\pm0.07)\times10^{14}$ m^{-2} and $(1.03\pm0.05)\times10^{14}$ m^{-2} for HTL/perovskite and perovskite/ETL interfaces, respectively. For the regular quality PSCs, the interface defects are in the range from 10^{13} m^{-2} to 10^{15} m^{-2} depending on the film quality [62]. Thus, a value below 10^{14} m^{-2} should be considered as a low defect concentration.

The analysis of PSC would not be completed if we focus only on FF. In general, we should analyze all photovoltaic parameters separately for better readability but they are intrinsically related to each other. Fig. 3d shows V_{oc} as a function of light intensity which allows the calculation of the ideality parameter (n_{id}) [87]. The value of n_{id} can also give detailed information about the dominant recombination process [88]. In the sample, the ideality factor is closer to 2 which would suggest the bulk recombination processes as a dominant one. However, the V_{oc}=1071 mV at 1 sun and the losses are not very high.

Therefore, the conclusion is that the bulk recombination process dominates in the sample.

3.2. The interface band–bending effect

The energy levels used for calculations are presented in Table 2. However, the edges of conduction and valence bands in samples could not be simply explained with the flat energy levels and the Fermi level pinning might appear in the perovskite absorber film [89]. The contact of the perovskite with the metal precursor can lead to the reduction of tin oxide and to the decomposition of a perovskite material. This phenomenon might occur locally, where PCBM does not fully cover the perovskite film. The thickness of a PCBM layer is optimized toward improvement of transport properties, thus it is most often chosen to be as thin as possible. Therefore, it is very likely that SnO_2 would find a pinpoint, where it would locally make a junction with a perovskite layer. Thus, the energetical band–bending might be observed for a direct contact of SnO_2 with a double–cation perovskite. The physical explanation of the band–bending effect is related to the formation of a junction between these two materials. We could describe it as the up–shift of the perovskite Fermi level and the down–shift of the SnO_2 Fermi level at the perovskite/SnO_2 interface. The energetical shift is explained with a higher donor doping of SnO_2 if compared to the perovskite material. Thus, although we have successfully simulated experimental results without considering the band–bending effect, in the following, we will discuss how this effect can affect the operation of the perovskite solar cell.

The diagram in Fig. 4a shows an energy alignment calculated under SC conditions for the front side of illumination. We have been able to simulate this effect by using few nanometers of a perovskite layer with down–shifted conduction and valence bands. As a consequence, a quantum well is created at the PCBM/perovskite interface. This would mimic the perovskite solar cell, where SnO_2 has a direct contact with the absorber layer. Fig. 4b shows the results of the J–V characteristics simulated under 1 sun conditions for different levels of the band–bending. It can be noticed that a higher level of the band–bending

process at the perovskite/ETL interface decreases FF, and also leads to an S–shape effect [90]. Also, the J–V characteristics start to resemble experimental results with SnO_2 prepared directly on the top of a perovskite film [39]. This proves the same mechanism of degradation but observed locally due to the partial coverage of a perovskite film with a PCBM layer. The band–bending mechanism also affects the slope of the J–V characteristics above OC and slightly increases V_{oc}. This observation has been already reported for organic solar cells [93]. Also, it is noticed that the band–bending process changes negligibly J_{sc}. However, the effect drastically affects FF at high illumination, see Fig. 4c. This is similar to an increase in the series resistance of the cell. The rise of an energy barrier actually lowers the extraction properties which increases the interface resistance of PSC. Interestingly, for a higher band–bending, we start to observe a non–linear behavior of V_{oc} which decreases mostly for lower light intensities, as shown in Fig. 4d. The physical explanation of this phenomenon seems to be related as an appearance of an additional shunt resistance in the device. This is especially visible at the lowest light intensity, where both V_{oc} and FF decrease drastically. Apparently, the increase of the band–bending effect at the perovskite/ETL interface acts as an additional loss channel for charge carriers, where their concentration is low (at the low light intensity).

Additionally, we have studied theoretically how the ETL interface defect density and the changing of the band–bending level can influence four photovoltaic parameters. Fig. 5 shows these dependencies for a sample illuminated from the front side, whereas Fig. 6 presents results for the rear side. Simulations have been made with the same values as in Table 2 but the ETL interface defect density changes here from 10^{14} m^{-2} to 10^{16} m^{-2}. We can see that all photovoltaic parameters have constant values for lower densities and a smaller height of band–bending. As a consequence, two–dimensional plateaus appear at the left–down corners in all parts of Fig. 5 and Fig. 6. In the case of the front illuminated side, areas of these plateaus are visibly greater than for the rear side. This is mostly related to the self–doping of a perovskite layer which leads to higher FF from the front side in comparison to the rear measurement side [91].

It is visible especially for J_{sc}, where this parameter is constant in the whole ETL density range (for depths of the interface quantum well lower than 220 meV). The increase of both the ETL interface defect density and the band–bending level causes a monotonic decrease of PCE and FF for both illuminated sides and the same effect for J_{sc}, when the light shines on the rear side. However, if the band–bending level is above ∼230 meV (the front side) and ∼320 meV (the rear side), values of these three photovoltaic parameters become independent of the ETL defect density. The V_{oc} indicates a similar behavior for the front side but we can see visible irregularities for higher levels of the band–bending. In general, the photovoltaic behavior of the device illuminated from the front side in respect to the defect concentration and the band–bending level is as expected. Meaning, the interface recombination controls mostly V_{oc}, especially in a higher regime of the defect concentration. The band–bending similarly appears to affect V_{oc} but it simultaneously impacts other photovoltaic parameters. This is because the band–bending influences both the charge carrier recombination and the transportation losses. However, the impact from the front side even thought both these parasitic processes are located on the rear side can be explained with a long lifetime of charge carriers in a perovskite material [92]. In the case of the second illuminated side, it is observed that V_{oc} rises monotonically with an increase of the band–bending level and reaches a maximal value when an interface quantum well is the deepest. Only for this case, the maximum of this photovoltaic parameter is not located on a two–dimensional plateau and has a greater value for the rear side. As it has been shown in [93], the V_{oc} can increase with a certain increasing of the band–bending due to the change of a vacuum level near the donor/acceptor interface. Seemingly, the same effect occurs in a perovskite solar cell, where the band–bending level changes its value at the perovskite/ETL interface.

Now, we will focus on the physical interpretation of the results presented in Fig. 5 and Fig. 6. Firstly, differences observed for the front and the rear sides can be partly explained based on the different optical losses for the illuminated sides, see the EQE results in Fig. 1c. Secondly, electrical properties can be

understood if we consider the ideality factor obtained for V_{oc}. Fig. 7 shows n_{id} as a function of the ETL interface defect density and the band–bending level for a sample illuminated from both sides. We observe that this factor starts to decrease with the increase of both the defect density and the height of the band–bending. This fact can be explained with an interface recombination mechanism. Next, when the depth of an interface quantum well becomes larger than ∼220 meV, then the n_{id} increases to a value above 4 at the level of 300 meV and decreases for higher levels. This behavior is practically independent of the ETL defect density. It has been experimentally demonstrated [94] that perovskite solar cells with inhomogeneous interfaces can be characterized by a very high n_{id} equal to 5. Thus, a value above 4 obtained in these calculations indicates a level of inhomogeneity. The observed decrease of n_{id} above 300 meV can be explained that charge carriers, which accumulate in a deep quantum well, are located close to the interface deep states and have a high probability to recombine through these states.

4. Conclusions

In this work, semitransparent PSCs with the tin oxide buffer layer have been studied. Using the light intensity measurements and numerical simulations, we identified the transportation and recombination effects. Additionally, the band–bending effect, which can appear at the ETL/perovskite interface, has been simulated and discussed. This phenomenon occurs when the solution processed PCBM layer might not fully cover the perovskite film. Our findings of the dominant electrical losses should lead to further optimization of high stability PSCs.

5. CRediT authorship contribution statement

Jędrzej Szmytkowski: Methodology, Validation, Formal analysis, Writing – Original Draft, Supervision, Project administration. **Yulia Galagan:**

Conceptualization, Methodology, Validation, Writing – Review & Editing, Supervision, Project administration, Funding acquisition. **Damian Glowienka:** Conceptualization, Methodology, Software, Validation, Formal analysis, Investigation, Resources, Writing – Original Draft, Project administration, Funding acquisition.

6. Declaration of Competing Interest

The authors declare that they have no known competing financial interests or personal relationships that could have appeared to influence the work reported in this paper.

7. Data availability

Data will be made available on request.

8. Acknowledgments

This research was funded in part by National Science Centre, in cooperation with the M–ERA.NET 3 Call 2021 for the grant number 2021/03/Y/ST5/00233. This project has received funding from the European Unions Horizon 2020 research and innovation program under grant agreement No 958174. The authors wish to thank the Academic Computer Centre (CI TASK) in Gdańsk for providing the opportunity to carry out calculations.

References

[1] C. Ballif, F.–J. Haug, M. Boccard, P.J. Verlinden, G. Hahn, Status and perspectives of crystalline silicon photovoltaics in research and industry, Nature Reviews Materials 7 (2022) 597–616.

[2] N. Papez, R. Dallaev, S. Talu, J. Kastyl, Overview of the current state of gallium arsenide–based solar cells, Materials 14 (2021) 3075.

[3] M. Gloeckler, I. Sankin, Z. Zhao, CdTe solar cells at the threshold to 20% efficiency, IEEE J. Photovolt. 3 (2013) 1389–1393.

[4] N. Mufti, T. Amrillah, A. Taufiq, Sunaryono, Aripriharta, M. Diantoro, Zulhadjri, H. Nur, Review of CIGS–based solar cells manufacturing by structural engineering, Solar Energy 207 (2020) 1146–1157.

[5] S. Sinha, D.K. Nandi, P.S. Pawar, S.–H. Kim, J. Heo, A review on atomic layer deposited buffer layers for Cu(In,Ga)Se_2 (CIGS) thin film solar cells: Past, present, and future, Solar Energy 209 (2020) 515–537.

[6] T. Chargui, F. Lmai, M. AL–Hattab, O. Bajjou, K. Rahmani, Experimental and numerical study of the CIGS/CdS heterojunction solar cell, Opt. Mater. 140 (2023) 113849.

[7] Y. Cui, R. Deng, G. Wang, D. Pan, A general strategy for synthesis of quaternary semiconductor Cu_2MSnS_4 (M = Co^{2+}, Fe^{2+}, Ni^{2+}, Mn^{2+}) nanocrystals, J. Mater. Chem. 22 (2012) 23136–23140.

[8] S.R. Meher, L. Balakrishnan, Z.C. Alex, Analysis of Cu_2ZnSnS_4/CdS based photovoltaic cell: A numerical simulation approach, Superlattices Microstruct. 100 (2016) 703–722.

[9] C. Nefzi, M. Souli, Y. Cuminal, N. Kamoun–Turki, Effect of sulfur concentration on structural, optical and electrical properties of Cu_2FeSnS_4 thin films for solar cells and photocatalysis applications. Superlattices Microstruct. 124 (2018) 17–29.

[10] M. Al–Hattab, E. Oublal, Y. Chrafih, L. Moudou, O. Bajjou, M. Sahal, K. Rahmani, Novel simulation and efficiency enhancement of eco–friendly Cu_2FeSnS_4/c–silicon tandem solar device, Silicon (2023), https://doi.org/10.1007/s12633-023-02582-5.

[11] S. Mandati, N. Juneja, A. Katerski, A. Jegorove, R. Grzibovskis, A. Vembris, T. Dedova, N. Spalatu, A. Magomedov, S. Karazhanov, V. Getautis,

M. Krunks, I.O. Acik, 4.9% efficient Sb_2S_3 solar cells from semitransparent absorbers with fluorene–based thiophene–terminated hole conductors, ACS Appl. Energy Mater. 6 (2023) 3822–3833.

[12] N. Shrivastav, V. Yadav, S. Bhattarai, J. Madan, M.K. Hossain, D.P. Samajdar, D.K. Dwivedi, R. Pandey, Two–terminal tandem solar cell with Sb_2S_3/Sb_2Se_3 absorber pair: achieving 14 % power conversion efficiency, Phys. Scr. 98 (2023) 115110.

[13] L.X. Chen, Organic solar cells: Recent progress and challenges, ACS Energy Lett. 4 (2019) 2537–2539.

[14] J. Gong, K. Sumathy, Q. Qiao, Z. Zhou, Review on dye–sensitized solar cells (DSSCs): Advanced techniques and research trends, Renew. Sustain. Energy Rev. 68 (2017) 234–246.

[15] T.M. Brenner, D.A. Egger, L. Kronik, G. Hodes, D. Cahen, Hybrid organic–inorganic perovskites: low–cost semiconductors with intriguing charge–transport properties, Nature Reviews Materials 1 (2016) 15007.

[16] D.A. Egger, A.M. Rappe, L. Kronik, Hybrid organic–inorganic perovskites on the move, Acc. Chem. Res. 49 (2016) 573–581.

[17] W. Li, Z. Wang, F. Deschler, S. Gao, R.H. Friend, A.K. Cheetham, Chemically diverse and multifunctional hybrid organic–inorganic perovskites, Nature Reviews Materials 2 (2017) 16099.

[18] National Renewable Energy Laboratory (NREL), Chart of Best Research–Cell Efficiencies. Available online: https://www.nrel.gov/pv/assets/images/efficiency-chart.png (accessed on 18 10 2023).

[19] R.G. Charles, A. Doolin, R. Garcia–Rodriguez, K.V. Villalobos, M.L. Davies, Circular economy for perovskite solar cells – drivers, progress and challenges, Energy Environ. Sci. 16 (2023) 3711–3733.

[20] S. Rahmany, L. Etgar, Semitransparent perovskite solar cells, ACS Energy Lett. 5 (2020) 1519–1531.

[21] M. Mujahid, C. Chen, J. Zhang, C. Li, Y. Duan, Recent advances in semitransparent perovskite solar cells, InfoMat. 3 (2021) 101–124.

[22] S. Lie, A. Bruno, L. H. Wong, L. Etgar, Semitransparent perovskite solar cells with $>$ 13% efficiency and 27% transperancy using plasmonic Au nanorods, ACS Appl. Mater. Interfaces 14 (2022) 11339–11349.

[23] J. Liang, C. Wang, Y. Wang, Z. Xu, Z. Lu, Y. Ma, H. Zhu, Y. Hu, C. Xiao, X. Yi, G. Zhu, H. Lv, L. Ma, T. Chen, Z. Tie, Z. Jin, J. Liu, All–inorganic perovskite solar cells, J. Am. Chem. Soc. 138 (2016) 15829–15832.

[24] Y. Li, C. Yang, W. Guo, Ti. Duan, Z. Zhou, Y. Zhou, All–inorganic perovskite solar cells featuring mixed group IVA cations, Nanoscale 15 (2023) 7249–7260.

[25] M. Al–Hattab, Y. Chrafih, E. Oublal, M. Sahal, L. Moudou, O. Bajjou, K. Rahmani, Ab initio investigation for solar technology on the optical and electronic properties of double perovskites Cs_2AgBiX_6 (X = Cl, Br, I), ECS J. Solid State Sci. Technol. 12 (2023) 094004.

[26] S. Bimli, V. Manjunath, S.R. Mulani, A. Miglani, O.S. Game, R.S. Devan, Theoretical investigations of all inorganic Cs_2SnI_6 double perovskite solar cells for efficiency $\sim$ 30 %, Solar Energy 256 (2023) 76–87.

[27] Y. Chrafih, M. Al–Hattab, K. Rahmani, Thermodynamic, optical, and morphological studies of the Cs_2AgBiX_6 double perovskites (X = Cl, Br, and I): Insights from DFT study, J. Alloys Compd. 960 (2023) 170650.

[28] C. Chen, S. Zhang, S. Wu, W. Zhang, H. Zhu, Z. Xiong, Y. Zhang, W. Chen, Effect of BCP buffer layer on eliminating charge accumulation for high performance of inverted perovskite solar cells, RSC Adv. 7 (2017) 35819–35826.

[29] W. Chen, Y. Wu, J. Liu, C. Qin, X. Yang, A. Islam, Y.-B. Cheng, L. Han, Hybrid interfacial layer leads to solid performance improvement of inverted perovskite solar cells, Energy Environ. Sci. 8 (2015) 629–640.

[30] A.K. Jena, Y. Numata, M. Ikegami, T. Miyasaka, Role of spiro–OMeTAD in performance deterioration of perovskite solar cells at high temperature and reuse of the perovskite films to avoid Pb–waste, J. Mater. Chem. A 6 (2018) 2219–2230.

[31] S.S. Mali, C.K. Hong, p–i–n/n–i–p type planar hybrid structure of highly efficient perovskite solar cells towards improved air stability: synthetic strategies and the role of p–type hole transport layer (HTL) and n–type electron transport layer (ETL) metal oxides, Nanoscale 8 (2016) 10528–10540.

[32] N. Shibayama, H. Kanda, T.W. Kim, H. Segawa, S. Ito, Design of BCP buffer layer for inverted perovskite solar cells using ideal factor, APL Mater. 7 (2019) 031117.

[33] J. Seo, S. Park, Y. Chan Kim, N.J. Jeon, J.H. Noh, S.C. Yoon, S.I. Seok, Benefits of very thin PCBM and LiF layers for solution–processed p–i–n perovskite solar cells, Energy Environ. Sci. 7 (2014) 2642–2646.

[34] X. Liu, H. Yu, L. Yan, Q. Dong, Q. Wan, Y. Zhou, B. Song, Y. Li, Triple cathode buffer layers composed of PCBM, C_{60}, and LiF for high–performance planar perovskite solar cells, ACS Appl. Mater. Interfaces 7 (2015) 6230–6237.

[35] H. Zhang, H. Azimi, Y. Hou, T. Ameri, T. Przybilla, E. Spiecker, M. Kraft, U. Scherf, C.J. Brabec, Improved high–efficiency perovskite planar heterojunction solar cells via incorporation of a polyelectrolyte interlayer, Chem. Mater. 26 (2014) 5190–5193.

[36] L. Chen, G. Wang, L. Niu, Y. Yao, Y. Guan, Y. Cui, Q. Song, High performance planar p–i–n perovskite solar cells based on a thin Alq_3 cathode buffer layer, RSC Adv. 8 (2018) 15961–15966.

[37] Q. Fu, X. Tang, B. Huang, T. Hu, L. Tan, L. Chen, Y. Chen, Recent progress on the long–term stability of perovskite solar cells, Adv. Sci. 5 (2018) 1700387.

[38] M. Najafi, V. Zardetto, D. Zhang, D. Koushik, M.S. Dörenkämper, M. Creatore, R. Andriessen, P. Poodt, S. Veenstra, Highly efficient and stable semi–transparent p–i–n planar perovskite solar cells by atmospheric pressure spatial atomic layer deposited ZnO, Solar RRL 2 (2018) 1800147.

[39] A.E.A. Bracesco, C.H. Burgess, A. Todinova, V. Zardetto, D. Koushik, W.M.M.E. Kessels, I. Dogan, C.H.L. Weijtens, S. Veenstra, R. Andriessen, M. Creatore, The chemistry and energetics of the interface between metal halide perovskite and atomic layer deposited metal oxides, J. Vacuum Sci. Technol. A 38 (2020) 063206.

[40] A.E. Shalan, Challenges and approaches towards upscaling the assembly of hybrid perovskite solar cells, Mater. Adv. 1 (2020) 292–309.

[41] Y. Li, L. Ji, R. Liu, C. Zhang, C.H. Mak, X. Zou, H.-H. Shen, S.-Y. Leu, H.-Y. Hsu, A review on morphology engineering for highly efficient and stable hybrid perovskite solar cells, J. Mater. Chem. A 6 (2018) 12842–12875.

[42] Y. Numata, Y. Sanehira, T. Miyasaka, Drastic change of surface morphology of cesium–formamidinium perovskite solar cells by antisolvent processing, ACS Appl. Energy Mater. 4 (2021) 1069–1077.

[43] D. Glowienka, D. Zhang, F. Di Giacomo, M. Najafi, S. Veenstra, J. Szmytkowski, Y. Galagan, Role of surface recombination in perovskite solar cells at the interface of HTL/$CH_3NH_3PbI_3$, Nano Energy 67 (2020) 104186.

[44] D. Glowienka, J. Szmytkowski, Numerical modeling of exciton impact in two crystalographic phases of the organo–lead halide perovskite ($CH_3NH_3PbI_3$) solar cell, Semicond. Sci. Technol. 34 (2019) 035018.

[45] A. Babayigit, J. D'Haen, H.-G. Boyen, B. Conings, Gas quenching for perovskite thin film deposition, Joule 2 (2018) 1205–1209.

[46] D. Zhang, M. Najafi, V. Zardetto, M. Dörenkämper, X. Zhou, S. Veenstra, L. Geerligs, T. Aernouts, R. Andriessen, High efficiency 4–terminal perovskite/c–Si tandem cells, Sol. Energy Mater. Sol. Cells 188 (2018) 1–5.

[47] M. Lundstrom, R. Schuelke, Modeling semiconductor heterojunctions in equilibrium, Solid State Electron. 25 (1982) 683–691.

[48] M.S. Lundstrom, R.J. Schuelke, Numerical analysis of heterostructure semiconductor devices, IEEE Trans. Electron Devices 30 (1983) 1151–1159.

[49] M. Gruber, B. Stickler, G. Trimmel, F. Schurrer, K. Zojer, Impact of energy alignment and morphology on the efficiency in inorganic–organic hybrid solar cells, Org. Electron. 11 (2010) 1999–2011.

[50] M. Georgioudakis, V. Plevris, A comparative study of differential evolution variants in constrained structural optimization, Frontiers in Built Environment 6 (2020) 102.

[51] J.A. Nelder, R. Mead, A simplex method for function minimization, The Computer Journal 7 (1965) 308–313.

[52] M. Newville, T. Stensitzki, D.B. Allen, M. Rawlik, A. Ingargiola, A. Nelson, Lmfit: non–linear least–square minimization and curve–fitting for python, 2016.

[53] H.J. Snaith, A. Abate, J.M. Ball, G.E. Eperon, T. Leijtens, N.K. Noel, S.D. Stranks, J.T.-W. Wang, K. Wojciechowski, W. Zhang, Anomalous hysteresis in perovskite solar cells, J. Phys. Chem. Lett. 5 (2014) 1511–1515.

[54] S.N. Habisreutinger, N.K. Noel, H.J. Snaith, Hysteresis index: a figure without merit for quantifying hysteresis in perovskite solar cells, ACS Energy Lett. 3 (2018) 2472–2476.

[55] J. Chen, N.-G. Park, Causes and solutions of recombination in perovskite solar cells, Adv. Mater. 31 (2019) 1803019.

[56] S.M. Kim, S.J. Park, H.H. Yoon, H.W. Choi, K.H. Kim, Preparation of ITO and IZO thin films by using facing target sputtering (FTS) method, J. Korean Phys. Soc. 55 (2019) 1996–2001.

[57] S. Arya, M. Riyas, A. Sharma, B. Singh, Prerna, P. Bandhoria, S. Khan, V. Bharti, Electrochemical detection of ammonia solution using tin oxide nanoparticles synthesized via sol–gel route, Appl. Phys. A 124 (2018) 538.

[58] L.-L. Deng, S.-L. Xie, C. Yuan, R.-F. Liu, J. Feng, L.-C. Sun, X. Lu, S.-Y. Xie, R.-B. Huang, L.-S. Zheng, High LUMO energy level $C_{60}(OCH_3)_4$ derivatives: electronic acceptors for photovoltaic cells with higher open–circuit voltage, Sol. Energy Mater. Sol. Cells 111 (2013) 193–199.

[59] A. Castro–Carranza, J.C. Nolasco, M. Estrada, R. Gwoziecki, M. Benwadih, Y. Xu, A. Cerdeira, L.F. Marsal, G. Ghibaudo, B. Iniguez, J. Pallares, Effect of density of states on mobility in small–molecule n–type organic thin–film transistors based on a perylene diimide, IEEE Electron Device Lett. 33 (2012) 1201–1203.

[60] N. Tsutsumi, K. Kinashi, K. Masumura, K. Kono, Photorefractive performance of poly(triarylamine)–based polymer composites: an approach from the photoconductive properties, J. Polym. Sci. B Polym. Phys. 53 (2015) 502–508.

[61] G. Chen, F. Zhang, M. Liu, J. Song, J. Lian, P. Zeng, H.-L. Yip, W. Yang, B. Zhang, Y. Cao, Fabrication of high–performance and low–hysteresis lead halide perovskite solar cells by utilizing a versatile alcohol–soluble bispyridinium salt as an efficient cathode modifier, J. Mater. Chem. A 5 (2017) 17943–17953.

[62] T.S. Sherkar, C. Momblona, L. Gil–Escrig, H.J. Bolink, L.J.A. Koster, Improving perovskite solar cells: insights from a validated device model, Adv. Energy Mater. 7 (2017) 1602432.

[63] G. Garcia–Belmonte, A. Munar, E.M. Barea, J. Bisquert, I. Ugarte, R. Pacios, Charge carrier mobility and lifetime of organic bulk heterojunctions analyzed by impedance spectroscopy, Org. Electron. 9 (2008) 847–851.

[64] R.C.I. MacKenzie, T. Kirchartz, G.F.A. Dibb, J. Nelson, Modeling nongeminate recombination in P3HT:PCBM solar cells, J. Phys. Chem. C 115 (2011) 9806–9813.

[65] D.B. Khadka, Y. Shirai, M. Yanagida, J.W. Ryan, K. Miyano, Exploring the effects of interfacial carrier transport layers on device performance and optoelectronic properties of planar perovskite solar cells, J. Mater. Chem. C 5 (2017) 8819–8827.

[66] G. Juska, K. Genevicius, N. Nekrasas, G. Sliauzys, G. Dennler, Trimolecular recombination in polythiophene: fullerene bulk heterojunction solar cells, Appl. Phys. Lett. 93 (2008) 143303.

[67] F. Brivio, K.T. Butler, A. Walsh, M. van Schilfgaarde, Relativistic quasiparticle self–consistent electronic structure of hybrid halide perovskite photovoltaic absorbers, Phys. Rev. B 89 (2014) 155204.

[68] D. Glowienka, F. Di Giacomo, M. Najafi, I. Dogan, A. Mameli, F.J.M. Colberts, J. Szmytkowski, Y. Galagan, Effect of different bromine sources on the dual cation mixed halide perovskite solar cells, ACS Appl. Energy Mater. 3 (2020) 8285–8294.

[69] J. Szmytkowski, D. Glowienka, M. Verger, H. Gorter, I. Dogan, W. Verhees, M. Najafi, S. Veenstra, Y. Galagan, Additive effect of bromides and chlorides on the performance of perovskite solar cells fabricated via sequential deposition, J. Power Sources 513 (2021) 230528.

[70] P. Tiwana, P. Docampo, M.B. Johnston, H.J. Snaith, L.M. Herz, Electron mobility and injection dynamics in mesoporous ZnO, SnO2, and TiO2 films used in dye–sensitized solar cells, ACS Nano 5 (2011) 5158–5166.

[71] S. Jeong, S. Seo, H. Park, H. Shin, Atomic layer deposition of a SnO2 electron–transporting layer for planar perovskite solar cells with a power conversion efficiency of 18.3%, Chem. Commun. 55 (2019) 2433–2436.

[72] M. Nagasawa, S. Shionoya, S. Makishima, Electron effective mass of SnO_2, J. Phys. Soc. Japan 20 (1965) 1093–1093.

[73] J. Song, E. Zheng, J. Bian, X.-F. Wang, W. Tian, Y. Sanehira, T. Miyasaka, Low–temperature SnO2–based electron selective contact for efficient and stable perovskite solar cells, J. Mater. Chem. A 3 (2015) 10837–10844.

[74] L.A.A. Pettersson, L.S. Roman, O. Inganäs, Modeling photocurrent action spectra of photovoltaic devices based on organic thin films, J. Appl. Phys. 86 (1999) 487–496.

[75] G.F. Burkhard, E.T. Hoke, M.D. McGehee, Accounting for interference, scattering, and electrode absorption to make accurate internal quantum efficiency measurements in organic and other thin solar cells, Adv. Mater. 22 (2010) 3293–3297.

[76] S. Manzoor, J. Häusele, K.A. Bush, A.F. Palmstrom, J. Carpenter, Z.J. Yu, S.F. Bent, M.D. McGehee, Z.C. Holman, Optical modeling of wide–bandgap perovskite and perovskite/silicon tandem solar cells using complex refractive indices for arbitrary–bandgap perovskite absorbers, Opt. Express 26 (2018) 7441–27460.

[77] D.A. Jacobs, Y. Wu, H. Shen, C. Barugkin, F.J. Beck, T.P. White, K. Weber, K.R. Catchpole, Hysteresis phenomena in perovskite solar cells: the many and varied effects of ionic accumulation, Phys. Chem. Chem. Phys. 19 (2017) 3094–3103.

[78] S. Ryu, D.C. Nguyen, N.Y. Ha, H.J. Park, Y.H. Ahn, J.-Y. Park, S. Lee, Light intensity–dependent variation in defect contributions to charge transport and recombination in a planar $MAPbI_3$ perovskite solar cell, Sci. Rep. 9 (2019) 19846.

[79] N. Thongprong, T. Supasai, Y. Li, I.-M. Tang, N. Rujisamphan, Insights into recombination processes from light intensity–dependent open–circuit voltages and ideality factors in planar perovskite solar cells, Energy Technol. 8 (2020) 1901196.

[80] S. Pang, D. Chen, C. Zhang, J. Chang, Z. Lin, H. Yang, X. Sun, J. Mo, H. Xi, G. Han, J. Zhang, Y. Hao, Efficient bifacial semitransparent perovskite solar cells with silver thin film electrode, Sol. Energy Mater. Sol. Cells 170 (2017) 278–286.

[81] A.K.K. Kyaw, D.H. Wang, V. Gupta, W.L. Leong, L. Ke, G.C. Bazan, A.J. Heeger, Intensity dependence of current–voltage characteristics and recombination in high–efficiency solution–processed small–molecule solar cells, ACS Nano 7 (2013) 4569–4577.

[82] G. Paul, S. Chatterjee, H. Bhunia, A.J. Pal, Self–doping in hybrid halide perovskites via precursor stoichiometry: to probe the type of conductivity through scanning tunneling spectroscopy, J. Phys. Chem. C 122 (2018) 20194–20199.

[83] Y. Hu, L. Song, Y. Chen, W. Huang, Two–terminal perovskites tandem solar cells: recent advances and perspectives, Solar RRL 3 (2019) 1900080.

[84] W. Shockley, H.J. Queisser, Detailed balance limit of efficiency of p–n junction solar cells, J. Appl. Phys. 32 (1961) 510–519.

[85] X. Ren, Z. Wang, W.E.I. Sha, W.C.H. Choy, Exploring the way to approach the efficiency limit of perovskite solar cells by drift–diffusion model, ACS Photonics 4 (2017) 934–942.

[86] Z. Ni, C. Bao, Y. Liu, Q. Jiang, W.-Q. Wu, S. Chen, X. Dai, B. Chen, B. Hartweg, Z. Yu, Z. Holman, J. Huang, Resolving spatial and energetic distributions of trap states in metal halide perovskite solar cells, Science 367 (2020) 1352–1358.

[87] D. Cheyns, J. Poortmans, P. Heremans, C. Deibel, S. Verlaak, B.P. Rand, J. Genoe, Analytical model for the open–circuit voltage and its associated resistance in organic planar heterojunction solar cells, Phys. Rev. B 77 (2008) 165332.

[88] W. Tress, M. Yavari, K. Domanski, P. Yadav, B. Niesen, J.P. Correa Baena, A. Hagfeldt, M. Graetzel, Interpretation and evolution of open–circuit voltage, recombination, ideality factor and subgap defect states during reversible light–soaking and irreversible degradation of perovskite solar cells, Energy Environ. Sci. 11 (2018) 151–165.

[89] T. Gallet, D. Grabowski, T. Kirchartz, A. Redinger, Fermi–level pinning in methylammonium lead iodide perovskites, Nanoscale 11 (2019) 16828–16836.

[90] S. Wilken, J. Parisi, H. Borchert, Role of oxygen adsorption in nanocrystalline ZnO interfacial layers for polymer–fullerene bulk heterojunction solar cells, J. Phys. Chem. C 118 (2014) 19672–19682.

[91] D. Glowienka, Y. Galagan, Light intensity analysis of photovoltaic parameters for perovskite solar cells, Adv. Mater. 34 (2022) 2105920.

[92] S.D. Stranks, G.E. Eperon, G. Grancini, C. Menelaou, M.J.P. Alcocer, T. Leijtens, L.M. Herz, A. Petrozza, H.J. Snaith, Electron–hole diffusion lengths exceeding 1 micrometer in an organometal trihalide perovskite absorber, Science 342 (2013) 341–344.

[93] S. Izawa, N. Shintaku, M. Hiramoto, Effect of band bending and energy level alignment at the donor/acceptor interface on open–circuit voltage in organic solar cells, J. Phys. Chem. Lett. 9 (2018) 2914–2918.

[94] A. Pockett, G.E. Eperon, T. Peltola, H.J. Snaith, A. Walker, L.M. Peter, P.J. Cameron, Characterization of planar lead halide perovskite solar cells by impedance spectroscopy, open–circuit photovoltage decay,

and intensity–modulated photovoltage/photocurrent spectroscopy, J. Phys. Chem. C 119 (2015) 3456–3465.

Table 1: Photovoltaic parameters for the representative sample measured from the front and the rear sides.

	front forward	front reverse	rear forward	rear reverse
J_{sc} [mA cm^{-2}]	18.89	19.19	17.98	18.35
V_{oc} [mV]	1055	1069	1056	1065
FF [%]	67.02	71.36	61.64	64.30
PCE [%]	13.36	14.64	11.71	12.57

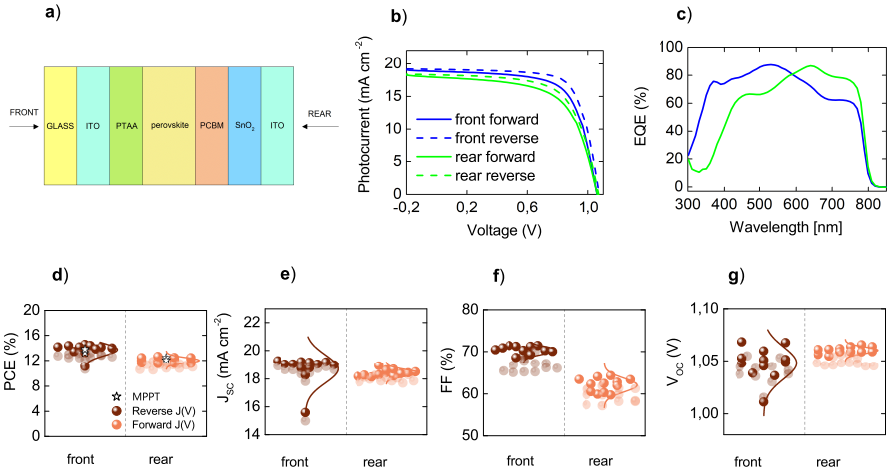

Figure 1: (a) Illustration of the PSCs sandwich structure consisting of the SnO_2 buffer layer (not to scale). (b) The J-V characteristics of the representative sample. The solid lines show the forward direction, whereas dash lines present the reverse scan. (c) The EQE results of the representative sample. Results for the front and the rear sides in parts (b)–(c) are plotted using blue and green lines, respectively. Photovoltaic parameters for all samples measured for both sides of illumination are presented in (d) PCE, (e) J_{sc}, (f) FF and (g) V_{oc}. Results for the front and the rear sides in parts (d)–(g) are given by red and orange symbols, respectively.

Table 2: Parameters applied in the simulations. Their values for holes are written in brackets and for electrons without brackets. Parameters given with an error are results of fitting.

Name	Unit	PTAA	2C perovskite	PCBM	SnO_2
Thickness	nm	14	535	40	45
Permittivity		2.67	24.1	3.75	9.86
Mobility	$cm^2\ V^{-1}\ s^{-1}$	(0.006)	9 (9)	0.002	0.003
Capture rate	$10^{-14}\ m^3\ s^{-1}$	-	1 (1)	-	-
Auger coefficient	$10^{-40}\ m^6\ s^{-1}$	-	1.55 (1.55)	-	-
Langevin prefactor		-	1.7×10^{-5}	-	-
Energy level	eV	(-5.35)	-3.88 (-5.44)	-3.90	-3.90
Doping concentration	m^{-3}	(0)	$(1\pm0.01)\times10^{21}$	0	10^{22}
Effective density of states	m^{-3}	2.5×10^{25}	10^{24}	2.5×10^{25}	2.5×10^{25}
Bulk trap density	$10^{21}\ m^{-3}$	-	7.23 (7.23)±0.09	-	-
HTL interface trap density	$10^{14}\ m^{-2}$	(1.09±0.07)	-	-	-
ETL interface trap density	$10^{14}\ m^{-2}$	-	-	1.03±0.05	-
Series resistance	$\Omega\ cm^2$		7.52±0.08		
Shunt resistance	$10^6\ \Omega\ cm^2$		1.80±0.22		

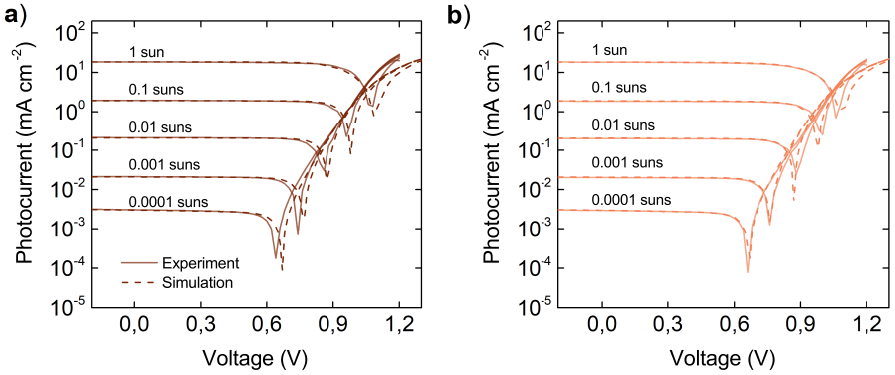

Figure 2: The J–V experimental (dark red and light red solid lines) and simulation (dark red and light red dash lines) characteristics measured under different light intensities from (a) the front and (b) the rear sides.

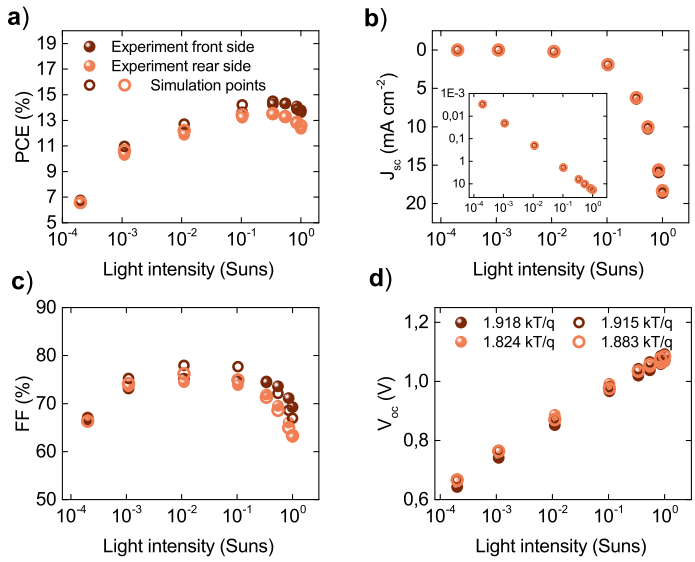

Figure 3: Photovoltaic experimental (closed symbols) and simulation (open symbols) results for different illuminations measured from the front (dark red symbols) and the rear (light red symbols) sides for the representative sample. (a) PCE, (b) J_{sc} with an inset having log–log scale, (c) FF and (d) V_{oc}.

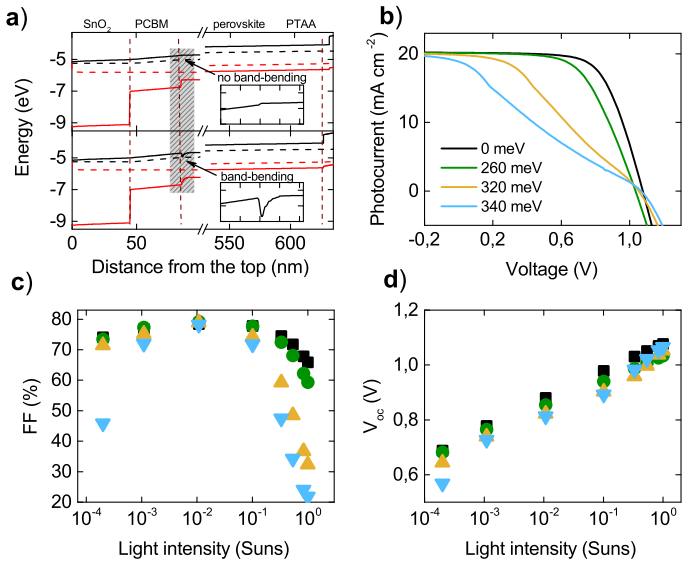

Figure 4: Simulation results (the front side) to show the effect of a band–bending with (a) an energy alignment in space, (b) the J–V results under 1 sun, (c) FF under different light intensities, and (d) V_{oc} under different light intensities. Part (a) is splitted into the upper part (without the band–bending effect) and the lower one (with 260 meV band–bending effect). Parts (b)–(d) show the results for different heights of the band–bending equal to 0 meV (black line or symbol), 260 meV (green line or symbol), 320 meV (yellow line or symbol) and 340 meV (blue line or symbol).

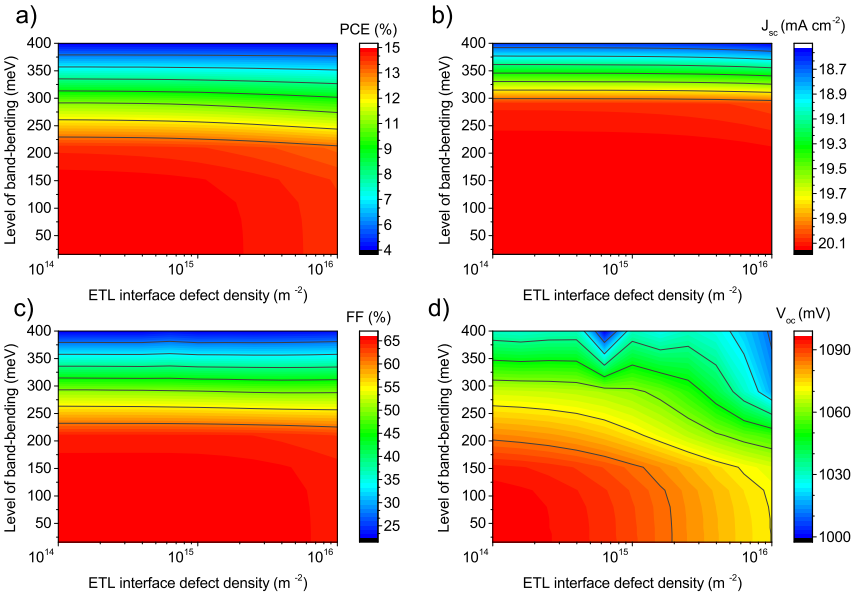

Figure 5: Four photovoltaic parameters as a function of the ETL interface defect density and the band–bending level for a sample illuminated from the front side. (a) PCE, (b) J_{sc}, (c) FF, (d) V_{oc}.

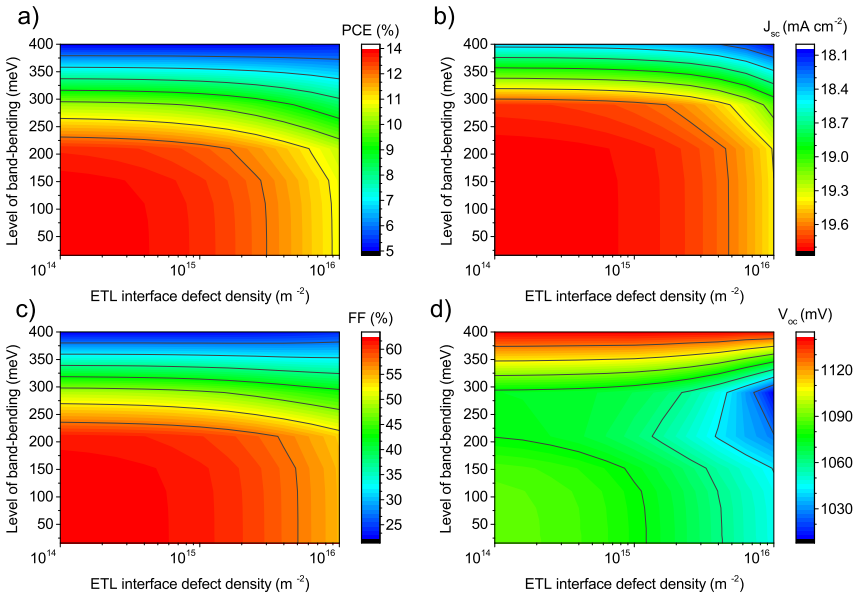

Figure 6: Four photovoltaic parameters as a function of the ETL interface defect density and the band–bending level for a sample illuminated from the rear side. (a) PCE, (b) J_{sc}, (c) FF, (d) V_{oc}.

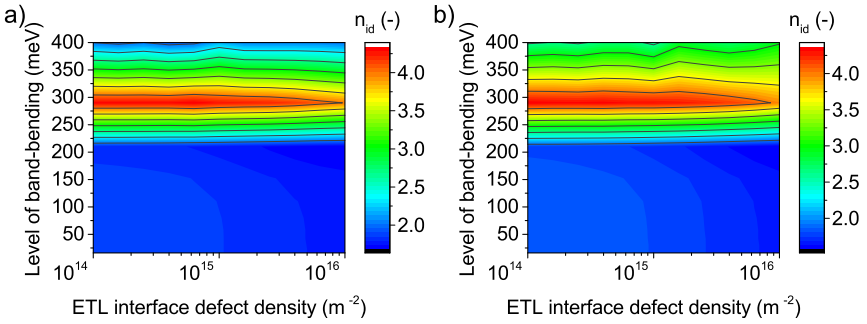

Figure 7: Ideality factors as a function of the ETL interface defect density and the band–bending level for a sample illuminated from (a) the front side and (b) the rear side.